
CRAMÉR-RAO BOUND-INFORMED TRAINING OF NEURAL NETWORKS FOR QUANTITATIVE MRI

Xiaoxia Zhang[†], Quentin Duchemin[†], Kangning Liu[†], Sebastian Flassbeck, Cem Gultekin,

Carlos Fernandez-Granda, Jakob Assländer

ABSTRACT

Neural networks are increasingly used to estimate parameters in quantitative MRI, in particular in *magnetic resonance fingerprinting*. Their advantages over the gold standard *non-linear least square fitting* are their superior speed and their immunity to the non-convexity of many fitting problems. We find, however, that in heterogeneous parameter spaces, i.e. in spaces in which the variance of the estimated parameters varies considerably, good performance is hard to achieve and requires arduous tweaking of the loss function, hyper parameters, and the distribution of the training data in parameter space. Here, we address these issues with a theoretically well-founded loss function: the Cramér-Rao bound (CRB) provides a theoretical lower bound for the variance of an unbiased estimator and we propose to normalize the squared error with respect to CRB. With this normalization, we balance the contributions of hard-to-estimate and not-so-hard-to-estimate parameters and areas in parameter space, and avoid a dominance of the former in the overall training loss. Further, the CRB-based loss function equals one for a maximally-efficient unbiased estimator, which we consider the ideal estimator. Hence, the proposed CRB-based loss function provides an absolute evaluation metric. We compare a network trained with the CRB-based loss with a network trained with the commonly used means squared error loss and demonstrate the advantages of the former in numerical, phantom, and in vivo experiments.

Keywords quantitative MRI, objective function, deep learning, parameter estimation, magnetic transfer (MT), magnetic fingerprinting (MRF).

[†] Xiaoxia Zhang, Quentin Duchemin, and Kangning Liu contributed equally to this work.

X. Zhang, S. Flassbeck, J. Assländer, are with the NYU School of Medicine, Dept. of Radiology, NY, NYC. (e-mails: xiaoxia.zhang@nyulaonge.org, Sebastian.Flassbeck@nyulangone.org, Jakob.Asslaender@nyulangone.org)

Q. Duchemin, is with LAMA, Univ Gustave Eiffel, Univ Paris Est Creteil, CNRS, F-77447 Marne-la-Vallée, France. (e-mail:quentin.duchemin@univ-eiffel.fr)

K. Liu is with NYU Center for Data Science, NY, NYC. (e-mail:kangning.liu@nyu.edu)

C. Gultekin is with NYU Courant Institute of Mathematical Sciences, NY, NYC. (e-mail:cg3306@nyu.edu)

C. Fernandez-Granda is with NYU Center for Data Science and Courant Institute of Mathematical Sciences, NY, NYC. (e-mail:cfgranda@cims.nyu.edu)

This research was supported by the grant NIH/NIBIB R21 EB027241 and was performed under the rubric of the Center for Advanced Imaging Innovation and Research, a NIBIB Biomedical Technology Resource Center (NIH P41 EB017183)

1 Introduction

Quantitative MRI (qMRI) characterizes the spin physics in biological tissue with the aim to provide quantitative biomarkers for pathological changes [8, 42, 31]. qMRI entails fitting a biophysical model to a signal curve, and this model fitting is usually a non-convex problem, which is traditionally solved via non-linear least square (NLLS) fitting. Besides the risk of this iterative algorithm to get stuck in a local minimum, NLLS is often prohibitively slow for clinical routine imaging [27]. Computation speed is particularly problematic for complex transient-state models that have been popularized by Magnetic Resonance Fingerprinting (MRF) [30].

MRF outsources the slow simulations to the precomputation of a dictionary, which is then matched to the measured signal. This approach equals a brute force grid search, which also overcomes the issue of a non-convex optimization landscape. Although dictionary matching ensures finding the global optimum within the simulated dictionary, it has known practical challenges, such as discretization errors and the so-called *curse of dimensionality*. The latter describes the exponentially increasing memory and computation time requirements with a growing number of biophysical parameters [20, 40].

The computational burden of dictionary matching can be reduced by singular value decomposition (SVD) and compressed sensing techniques [10, 50, 14, 32, 47]. Nonetheless, these improvements do not overcome the curse of dimensionality and the computational burden is prohibitive for models with many parameters, such as the magnetization transfer (MT) model used here, which has overall 8 parameters. In contrast, the curse of dimensionality can be overcome with dictionary-free regression methods [9, 34], as well as deep learning (DL). As a result, these methods are very fast once the network has been trained. As the parameter fitting in both of these methods is feed-forward, it cannot get stuck in local minima. Because of those advantages over NLLS fitting and dictionary matching, these methods gained a lot of attention recently, in particular DL [16, 15, 24, 44, 12, 23, 35, 20, 18, 40, 7]: e.g., the DRONE [12] method maps the magnitudes of fingerprints to T_1 and T_2 maps with a four-layer fully connected network (FCN). Virtue et al. [44] designed a three-layer FCN, which processes complex-valued data. During training, they augment the data with undersampling artifacts, which are heuristically derived from in vivo data. Additionally, convolutional neural networks [25, 23, 20] and recurrent neural networks [35] have been proposed to exploit the temporally local structure of the fingerprints. Inspired by the work of McGivney et al. [33], who showed that MRF dictionaries are often low rank, Golbabaee et al. [18] trained a neural network with a first layer fixed to the singular vectors associated with the highest singular values. In [40], image reconstruction is performed by solving a regularized version of an optimization problem with a low rank constraint, followed by a deep non-local residual convolutional neural network to restore parameter maps.

Most of the above described methods use the mean squared error (MSE) as the objective function during training, which aims to minimize the sum of the squared differences between each parameter and its estimate [24, 40, 12, 44, 35, 25, 23, 20, 18]. However, this loss has natural weaknesses for parameter estimation: different parameters are at different scales and have different dimensions. For example, T_1 values are about 10 times larger than T_2 . As a result, T_1 can dominate the MSE loss during the training of a network that jointly estimates both parameters [16, 15]. When estimating parameters of different physical dimensions, such as the fractional proton density m_0^s (cf. Section 2.3) and the relaxation times, using MSE as loss function becomes even more questionable from a physics perspective. Indeed, the use of MSE in this context violates the well-known homogeneity principle which states that two quantities with different dimensions cannot be added up.

These problems can be overcome with the mean relative absolute error as suggested in Refs. [16, 15, 19], or by training separate networks to estimate each parameter. Another problem is, however, not addressed by the mean relative absolute error: it is often easier to estimate one biophysical parameter within a specific range of parameters, than it is in other ranges. To give an example, the estimation of T_1 usually becomes increasingly difficult at short T_2 -times as this reduces the overall signal to noise ratio. While this example is rather pictorial, the ease of parameter estimation is not always intuitive and gives rise to the same problem described above: the MSE is dominated by areas in parameter space where the estimate has large errors and these areas are usually not the ones of interest, in particular when using a pulse sequence that was optimized for a certain area in parameter space [51, 5].

In this paper, we introduce a theoretically grounded loss function that ensures close to optimal performance even in heterogeneous and high-dimensional parameter spaces. We will demonstrate that the proposed loss function fulfills these requirements by normalizing the squared error of each estimate with respective Cramér-Rao bound (CRB) [38, 13], a theoretical lower bound for the variance of an unbiased estimator.

In Section 2 we introduce the CRB-weighted loss function while connecting neural-network (NN)-based parameter estimation back to signal processing theory. In Section 3, we show that our approach can jointly and efficiently predict multiple parameters in a high-dimensional parameter space, and we compare it to the commonly used MSE loss. We elaborate the advantages and disadvantages of the proposed loss function in Section 4. Code for replicating the proposed

work will be available on <https://github.com/quentin-duchemin/MRF-CRBLoss>. The most updated version of code for fingerprints simulation used in this paper is available on <https://github.com/JakobAsslaender/MRIgeneralizedBloch.jl>.

2 Method

2.1 The Cramér-Rao bound (CRB)

First, we recap the definition of the Cramér-Rao Bound and some of its properties that are useful for this paper. We consider a biophysical model with P parameters and we denote the fingerprint corresponding to any set of tissue parameters $(\theta_1, \dots, \theta_P) \in \mathbb{R}^P$ by $\mathbf{x}(\theta_1, \dots, \theta_P) \in \mathbb{C}^d$, where d is the number of data points in the fingerprint. We assume that for some tissue parameters $(\theta_1, \dots, \theta_P)$ we observe a normally distributed random vector X with mean $\mathbf{x}(\theta_1, \dots, \theta_P)$ and with covariance matrix $\sigma^2 \text{Id}_d$ where $\sigma^2 > 0$ and $\text{Id}_d \in \mathbb{R}^{d \times d}$ is the identity matrix. We want to estimate θ_i (for some $i \in [P]$) from X . In general, an estimator of θ_i cannot minimize the MSE uniformly in $(\theta_1, \dots, \theta_P)$, because of the bias-variance decomposition. However, if one restricts itself to the class of unbiased estimators, then the search for an estimator with minimal MSE is reduced to the problem of variance minimisation. The CRB provides a universal limit for the noise variance of any unbiased estimator of the parameter θ_i [38, 13].

We define the Fisher information matrix $F \in \mathbb{C}^{P \times P}$ at a point in parameter space $(\theta_1, \dots, \theta_P)$ whose entries are

$$F_{i,j} := \frac{1}{\sigma^2} \left[\frac{\partial \mathbf{x}(\theta_1, \dots, \theta_P)}{\partial \theta_i} \right]^H \frac{\partial \mathbf{x}(\theta_1, \dots, \theta_P)}{\partial \theta_j},$$

where the superscript H denotes the complex conjugate transposed. The Cramér-Rao bound associated with the i^{th} parameter is defined as: $\text{CRB}_i(\theta_1, \dots, \theta_P) = (F^{-1})_{i,i}$. Given some $i \in [P]$, the noise variance of any unbiased estimator of θ_i based on the observation X is at least as large as the corresponding Cramér-Rao bound $\text{CRB}_i(\theta_1, \dots, \theta_P)$.

2.2 CRB-weighted MSE loss

Ultimately, we aim at training a neural network that estimates parameters with high accuracy and precision. High accuracy implies that the average of estimates over many noise realizations converges to the ground truth, i.e., the estimation has little-to-no bias. Precision analyzes the spread, i.e., the variance of estimates. From signal processing theory, we know that an unbiased estimator has a variance equal to or larger than the Cramér-Rao bound (CRB) (see Section 2.1), and we have shown previously that the CRB is a good predictor of the noise variance for MRF-like data when using a non-linear least square fitting approach [6]. We propose to normalize the squared error with respective CRB before averaging over all estimated parameters and all samples in the training data:

$$L_{\text{CRB}} = \frac{1}{P_e S} \sum_{s=1}^S \sum_{p_e=1}^{P_e} \frac{(\hat{\theta}_{p_e,s} - \theta_{p_e,s})^2}{\text{CRB}_{p_e}(\theta_{1,s}, \dots, \theta_{P,s})}. \quad (1)$$

Here, θ denotes a biophysical parameter, $\hat{\theta}$ its estimate, $s \in \{1, \dots, S\}$ runs over all samples in the training dataset, $p_e \in \{1, \dots, P_e\}$ over all parameters estimated by the network, and $p \in \{1, \dots, P\}$ over all parameters of the model. The distinction between P_e and P is made to allow for estimating only a subset of parameters, which can be done while still considering a fit of the full model. The key here is to vary all parameters in the training dataset. In this case, the CRB has to account for the derivatives of the signal with respect to all model parameters.

With this normalization, a maximally efficient unbiased estimator—which we consider the ideal estimator—has a loss of 1, which provides an absolute metric to evaluate a network’s performance. Further it addresses above mentioned drawbacks of the MSE loss function: A maximally efficient unbiased estimator has a loss of 1 not only when averaging over all estimated parameters and all samples in the training dataset, but the expectation value of the CRB of each parameter and sample of the training dataset is one. Thus, the CRB-weighted loss function suffers neither from being dominated by parameters with large values, nor by parameters that are difficult to estimate.

2.3 Biophysical model

In order to highlight the ability of our loss function to handle high-dimensional parameter spaces in which the difficulty to estimate parameters varies substantially, we use an 8-parameter magnetization transfer model [26]. It is based on Henkelman’s original two-pool spin model [22] that distinguishes between protons bound in water—the so-called *free pool*—and protons bound in macromolecules, such as proteins or lipids—the so-called *semi-solid pool*. The pulse sequence is designed such that the free pool remains in the hybrid state [6, 26]—a spin ensemble state that provides

a combination of robust and tractable spin dynamics with the ability to encode biophysical parameters with high signal-to-noise ratio (SNR) efficiency compared to steady-state MR experiments [6]. The model has the following parameters: An apparent T_1 relaxation time of both pools, T_2^f of the free and T_2^s of the semi-solid pool, the size of the semi-solid pool m_0^s , which is normalized by the sum $m_0^s + m_0^f = 1$, the exchange rate R_x between the two pools, the imperfectly calibrated B_0 and B_1 , and a complex-valued scaling factor M_0 .

2.4 Data simulation

We simulated fingerprints with a custom implementation in MATLAB (Mathworks, USA) with random sets of parameters with the following distributions: we used truncated Gaussian distributions with means and standard deviations of $m_0^s = 0.12 \pm 0.08$ while ensuring $m_0^s \geq 0$, $T_1 = (1.6 \pm 0.8)\text{s}$, $T_2^f = (0.1 \pm 0.2)\text{s}$ while ensuring $T_2^f \leq T_1$, $R_x = (44 \pm 20)/\text{s}$ while ensuring $R_x \geq 0$, $B_1/B_1^{\text{nominal}} = 1 \pm 0.3$. Further, we used a uniformly distributed $B_0 \in [-2\pi/T_R, 2\pi/T_R]$ where T_R is the repetition time.

With these distributions, we simulated 92,160 fingerprints for a training dataset, 10,240 for a validation, and 9,056 for our testing dataset #1. We performed a singular value decomposition of the training dataset and compressed all three datasets to the coefficients corresponding to the 13 largest singular values.

After computing the SVD, we multiplied the three datasets with a random scaling factor M_0 , which has a uniformly distributed absolute value $|M_0| \in [0.1, 1]$ and a complex phase uniformly distributed in the range $[0, 2\pi]$. We added complex valued Gaussian noise with a standard deviation of 0.01, which results in an overall SNR_{max} in the range 10 to 100, where we define SNR_{max} as the maximum achievable SNR, i.e. the SNR one would measure with $T_R \rightarrow +\infty$ and the echo time $T_E \rightarrow +0$ [3]. Note that we multiplied the fingerprints with a different M_0 and we added different noise realizations in each training epoch to reduce overfitting.

In addition to the randomly distributed testing dataset #1, we also conducted analyses on a regular grid for a simple visualization of certain performance metrics. This dataset #2 is limited to 2D slices that cut through the 8-dimensional parameter space: one slice varies m_0^s and T_1 and one varies T_1 and T_2^f while fixing other 6 parameters to the mean values used in the training sampling scheme.

2.5 Neural network design

As our quantitative MT model is more complex compared to the Bloch model used in previous NN-based MRF[24, 12, 18, 44, 40], we use a larger network with more capacity to capture the high-dimensional mapping functions. The network size was empirically selected to ensure accurate functional mapping while keeping the training time and memory requirements within limits. Our network consists of 14 fully-connected layers. Except for the output layer, each fully-connected layer is followed by group normalization [49] and rectifier linear units (ReLU) activation functions [2]. We incorporated skip connections [21] to avoid the vanishing gradient problem during training.

The network used here treats each voxel independently. The inputs of the network are the 13 complex-valued coefficients of the compressed training or testing data, split into real and imaginary parts and normalized to have an ℓ_2 -norm of 1. The outputs of the last layer are the estimated parameters of interest; in our case m_0^s , T_1 , and T_2^f as we consider these parameters to be the most relevant to our main target application multiple sclerosis and since we optimized the pulse sequence for this purpose [26]. The network is, however, also capable of estimating additional parameters, such as B_0 and B_1 , with the same training routine and architecture, modified to have more output channels (not shown here).

2.6 Training details

The weights of the network are initialized randomly and we used ADAM optimizer[28] with a batch size of 512. The learning rate was initially set to 0.01 and decayed by half every 40 epochs. We trained the network for 400 epochs, and observed good convergence. We trained two networks: one with proposed CRB-weighted loss (see (1)) and one with the commonly used MSE loss for comparison. We experimentally found this network is not very sensitive to hyper-parameters by searching the hyper-parameter space, therefore, we set them identical when train both networks.

2.7 Bias and variance analysis

In order to separate bias from noise in our performance analysis, we process each fingerprint of the two testing datasets with N different noise realizations for a given SNR_{max} . This allows us to calculate the bias of a parameter estimate

$$\hat{\theta}_{p_e, s}: \quad \text{bias}(\theta_{p_e, s}) = \bar{\theta}_{p_e, s} - \theta_{p_e, s}, \quad (2)$$

as well as the variance

$$\sigma^2(\theta_{p_e,s}) = \sum_{n=1}^N \frac{(\hat{\theta}_{n,p_e,s} - \bar{\theta}_{p_e,s})^2}{N}, \quad (3)$$

where $n \in \{1, \dots, N\}$ runs over all noise realizations, $\theta_{p_e,s}$ denotes the ground truth, $\hat{\theta}_{n,p_e,s}$ an estimate, and $\bar{\theta}_{p_e,s}$ the average of all N estimates of $\theta_{p_e,s}$.

In the same spirit, multiple noise realizations of a single fingerprint allow us to split the average loss of each fingerprint into a bias and a variance component:

$$\bar{L}_{\text{CRB}}(\theta_{p_e,s}) = \frac{\sum_{n=1}^N (\hat{\theta}_{n,p_e,s} - \theta_{p_e,s})^2}{N \cdot \text{CRB}_{p_e}(\theta_{1,s}, \dots, \theta_{P,s})} \stackrel{N \rightarrow +\infty}{=} \underbrace{\frac{(\bar{\theta}_{p_e,s} - \theta_{p_e,s})^2}{\text{CRB}_{p_e}(\theta_{1,s}, \dots, \theta_{P,s})}}_{\bar{L}_{\text{CRB}}^{\text{bias}}(\theta_{p_e,s})} + \underbrace{\frac{\sum_{n=1}^N (\hat{\theta}_{n,p_e,s} - \bar{\theta}_{p_e,s})^2}{N \cdot \text{CRB}_{p_e}(\theta_{1,s}, \dots, \theta_{P,s})}}_{\bar{L}_{\text{CRB}}^{\sigma^2}(\theta_{p_e,s})} \quad (4)$$

where $\bar{L}_{\text{CRB}}^{\text{bias}}(\theta_{p_e,s})$ and $\bar{L}_{\text{CRB}}^{\sigma^2}(\theta_{p_e,s})$ are the contributions of the bias and the variance to the average loss of each parameter and sample $\theta_{p_e,s}$, respectively. The bar indicates the loss averaged over multiple noise realizations.

Averaging the loss further over all estimated parameters p_e and samples or fingerprints s results in the overall loss with its two contributions:

$$\bar{L}_{\text{CRB}} = \underbrace{\sum_{p_e,s} \frac{\bar{L}_{\text{CRB}}^{\text{bias}}(\theta_{p_e,s})}{P_e \cdot S}}_{\bar{L}_{\text{CRB}}^{\text{bias}}} + \underbrace{\sum_{p_e,s} \frac{\bar{L}_{\text{CRB}}^{\sigma^2}(\theta_{p_e,s})}{P_e \cdot S}}_{\bar{L}_{\text{CRB}}^{\sigma^2}}. \quad (5)$$

Note that $\bar{L}_{\text{CRB}} = \sum_n L_{\text{CRB},n}/N$ connects this average loss back to the one used during training (Eq. (1)).

We used Eq. (5) to calculate the contributions of bias and variance to the CRB-loss for different SNR_{max} values by evaluating $N = 300$ noise realizations for each SNR_{max} . The same analysis was repeated for the MSE-loss without normalizing the CRB values in Eqs. (4). To further investigate those contributions of each parameter to the loss, we conducted this analysis based on each parameter separately for a specific SNR_{max} .

2.8 Phantom and in vivo scans

We built a magnetization transfer phantom with thermally cross-linked bovine serum albumin (BSA). We mixed BSA powder with distilled water in three different concentrations: 10%, 15%, and 20% of the overall sample weight. The mixtures were stirred at 30°C until the BSA was fully dissolved. We split each solution into two batches and doped one of them with 0.1mM MnCl_2 . We filled six plastic tubes with the resulting solutions and thermally cross-linked them in a water bath at approximately 90°C for 10 minutes. We note that the 10% BSA mixture without MnCl_2 was cross-linked separately as a trial run, which seemed to have resulted in somewhat inconsistent MT properties. We immersed the six tubes in a head-sized cylindrical container filled with doped water.

We scanned the phantom with our hybrid-state qMT sequence [26] on a 3T Prisma scanner (Siemens Healthineers, Erlangen, Germany) with a 20-channel head coil. The sequence acquires 3D data with 1mm isotropic resolution in approximately 12 minutes with a radial kosh-ball k-space trajectory, whose angles are incremented by 2D-golden angles [26, 17, 48, 11].

We further scanned an asymptomatic volunteer with approval of our institutional review board and after getting informed consent. For the in vivo scan, we used a 64-channel head-neck coil and we compressed the data to 20 virtual coils with a singular value decomposition.

We reconstructed both datasets with the *low rank inversion* described in Ref. [4], using the 13 singular vectors from above described SVD of the training data. We used the *BART* implementation of this reconstruction [41, 43] and added locally-low rank regularization to reduce undersampling artifacts and noise [41]. The 13 resulting coefficient images show minimal undersampling artifacts and we assume the residual artifacts and noise to be Gaussian distributed. Voxel-by-voxel, these 13 complex-valued coefficients, normalized to have an ℓ_2 -norm of 1, are fed into the neural networks for the parameter estimation.

To analyze the phantom data, we selected a central slice through the phantom and masked each tube separately. We eroded the out-most voxels to avoid partial-volume effects and performed a box-plot analysis. Thereafter, we compare parameters estimated with a non-linear least square fit (NLLS), with the neural network that was trained with the MSE loss, and with the neural network trained with the CRB-weighted loss.

3 Results

3.1 Convergence analysis

Fig. 1 reveals that the CRB-weighted loss indeed converges approximately to 1, which is a necessary (but not sufficient) condition of a maximally efficient unbiased estimator and, thus, provides an absolute evaluation metric. In contrast, the MSE-loss converges to a value that gives little insight in the performance of the network. Additionally, the CRB-loss converges virtually monotonously while the MSE-loss exhibits comparably strong fluctuations.

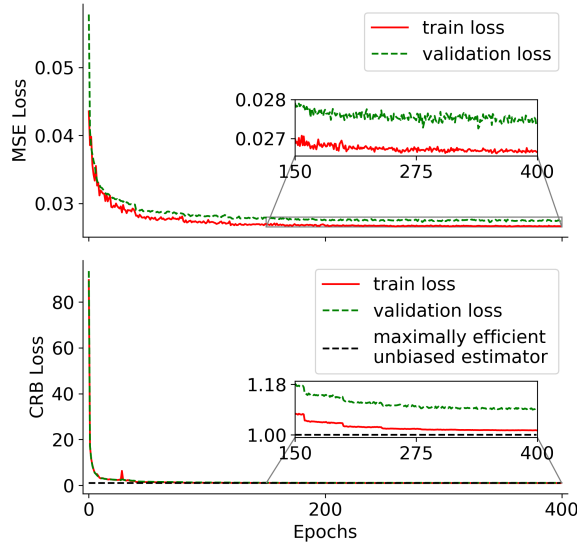


Figure 1: Convergence of the training and validation loss. The CRB-loss converges to approximately 1, which corresponds to the loss of a maximally efficient unbiased estimator, while the MSE-loss converges to a value that provides little insight in the performance of the network. The two curves result from separate networks trained with respective loss function.

3.2 Bias and variance analysis of the converged networks

In order to confirm that the network trained with the CRB-loss approximates a maximally efficient unbiased estimator, we performed three analyses. The first one aims at a visual analysis and uses the testing dataset #2 that lies on a regular grid. As the parameter space is 8-dimensional, this analysis is limited to single slices through this space. When using the network trained with the CRB-loss, the bias of the T_2^f estimation in a slice spanned by T_1 and T_2^f is small (Fig. 2b; 5.23ms on average) compared to the bias of the estimation with the MSE-based network (Fig. 2a; 14.1ms on average).

Comparing the standard deviation of estimates to the square root of the Cramér-Rao bound, we observe close concordance in the case of the network trained with the CRB-loss, while we observe substantial deviations for the network trained with the MSE-loss (Fig. 2c-e). In particular at short T_1 and long T_2^f times, the standard deviation of \hat{T}_2^f , estimated with the MSE-based network, is substantially larger compared to the square root of the CRB, indicating sub-optimal precision in addition to the large bias (Fig. 2a,c). In contrast, when using the network trained with the CRB loss, we find good agreement between standard deviation of the parameter estimates and the square root of the CRB itself, which indicates that this network approximates a maximally efficient unbiased estimator. Overall, the two networks have similar performance in estimating m_0^s and T_1 on the dataset #2 (cf. supplementary material), while we do observe a substantial difference in the performance in estimating T_2^f .

These findings are confirmed by an analysis of the test dataset #1, which covers the same volume in the 8D parameter space as the training data. The bias of m_0^s , visualized with histograms in Fig. 3, is overall smaller when using the CRB-based network in comparison to the MSE-based network. The same holds true for T_1 and T_2^f , as evident by the higher count in the bin centered around zero bias. This finding is, however, somewhat obscured by the opposite signs in the biases when comparing the two networks.

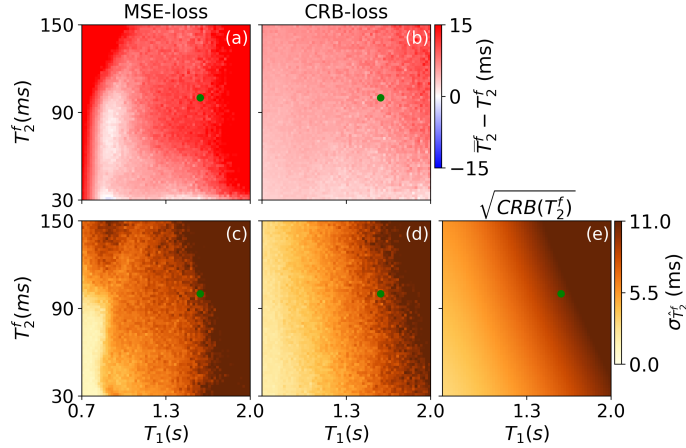


Figure 2: Bias (a,b) and standard deviation (c,d) of \hat{T}_2^f , estimated with the networks trained with the MSE-loss and CRB-loss, respectively. The standard deviation is compared to the square root of the Cramér-Rao bound (e), which provides a theoretical lower bound for an unbiased estimator. The green dots indicate the mean values of the corresponded parameters in the training dataset. The maps were generated with the test dataset #2.

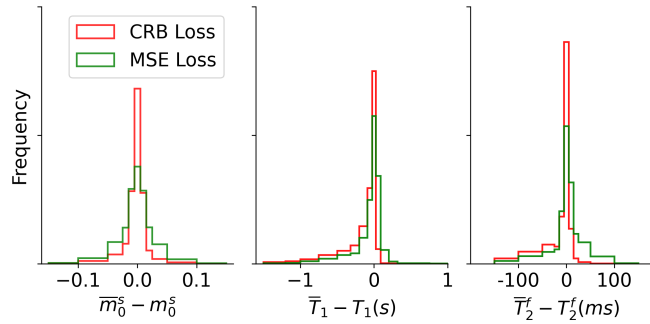


Figure 3: Bias analysis. The randomly sampled fingerprints in test dataset #1 were processed with 300 noise realizations ($\text{SNR}_{\max} = 50$) and the mean value is compared to the ground truth. Overall, one can observe a smaller bias when estimating the parameters with the network trained with the CRB-loss compared to the network trained with the MSE-loss.

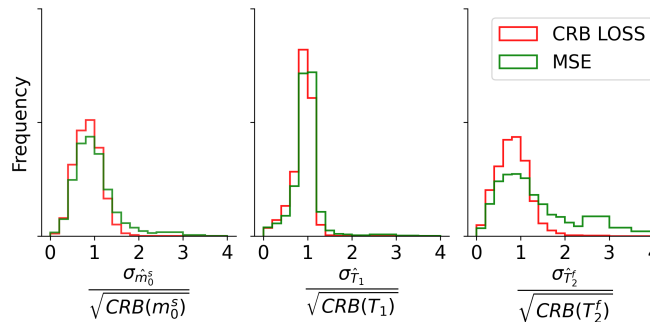


Figure 4: Standard deviation analysis. The randomly sampled fingerprints in test dataset #1 were processed with 300 noise realizations ($\text{SNR}_{\max} = 50$) and the standard deviation of the estimates is analyzed. Overall, one can observe a smaller variance when estimating the parameters with the CRB-based network compared to the network trained with the MSE-loss. A maximally efficient unbiased estimator has a standard deviation, divided by the square root of the CRB, of 1.

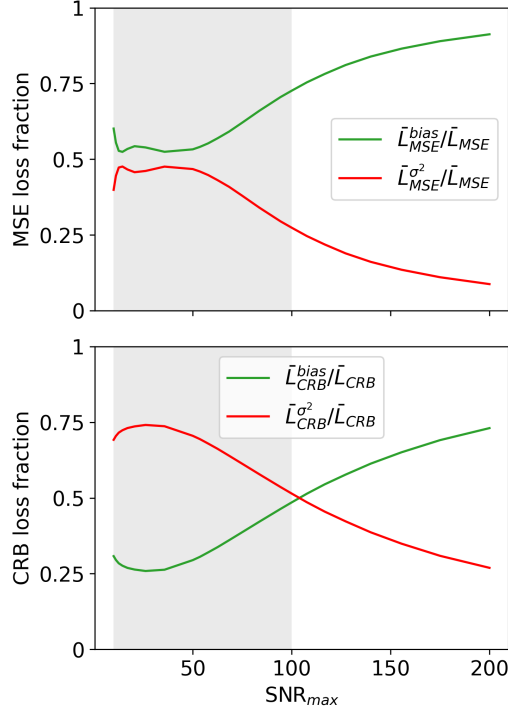


Figure 5: Bias and variance contributions to the loss. In case of the network trained with the MSE-loss, the bias dominates the overall loss. In contrast, the loss of the CRB-based network is dominated by the variance within the training range $\text{SNR}_{\max} \in [10, 100]$, highlighted by the gray shade. This decomposition of CRB-loss was performed with Eq. (5) on the test dataset #1.

Fig. 4 depicts the ratio of the estimates’ standard deviation and the square root of the CRB. For a maximally efficient unbiased estimator, this ratio is 1 and the network trained with the CRB-loss approximates this property well and better compared to the network trained with the MSE-loss, in particular in the estimation of T_2^f .

In the third analysis, we decomposed the loss with Eq. (5) into a bias and a variance component. In the case of the MSE-based network, the loss is dominated by the bias. In contrast, the loss of the CRB-based network is dominated by the variance within the training range of $\text{SNR}_{\max} \in [10, 100]$ and the bias component becomes dominant only at SNR_{\max} values outside of the training range (Fig. 5).

Taking a close look at the loss composition at $\text{SNR}_{\max} = 50$, which is roughly the SNR found in vivo, we find that the bias contributions are overall lower for the CRB-based network, with the exception of T_1 and T_2^f at very high CRB values (Fig. 6). This confirms that, at least for parameter combinations with moderate CRB values, the CRB-based network results on average in a smaller bias.

3.3 Phantom data

The improved performance of the network trained with the CRB-loss is confirmed by phantom experiments (Fig. 7). We estimated m_0^s , T_1 , and T_2^f for the samples with different BSA concentrations using the two neural networks, as well as a non-linear least square (NLLS) fitting algorithm, which we consider the gold standard. For virtually all samples, we found better agreement of the CRB-based network estimates with the NLLS results, compared to the MSE-based network estimates. For most samples, the estimates with the CRB-based network and the NLLS algorithm match within their interquartile range. The most pronounced deviations can be found in m_0^s , which has overall the highest CRB and is, thus, the most difficult one to estimate (not shown here). Estimates calculated with the MSE-based network are overall in good agreement with the NLLS fits as well. Yet, the deviations are somewhat larger compared to the CRB-based network. Further, analyzing the interquartile range as well as the overall range of estimates, we find that the CRB-based network has variations comparable to, and for many samples slightly smaller than the spread of NLLS estimates. In comparison, the spread of the MSE-based network estimates is larger for most samples.

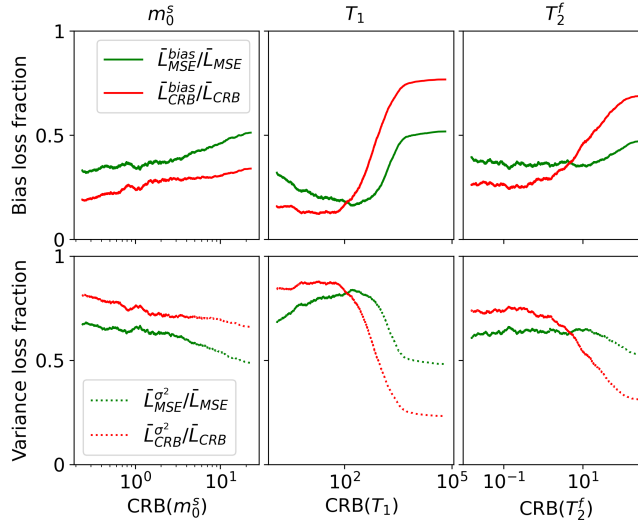


Figure 6: Bias and variance contributions to the loss. The CRB-based network results overall in a smaller bias compared to the MSE-based network, with the exception of T_1 and T_2^f at very high CRB-values, i.e. for parameter combinations that are hard to estimate. The decompositions of the loss were performed with Eqs. (4) and (5) on the test dataset #1 with $\text{SNR}_{\max} = 50$ and is further split into separate parameters.

3.4 In vivo data

The in vivo data paints largely the same picture: We find overall good agreement between both networks and the NLLS fits. For m_0^s , the relative deviations between the CRB-based network and NLLS is approximately 10% and the deviations for the MSE-based network are slightly larger. For the T_1 estimations, the MSE-based network performs slightly better, which is in line with our finding that the MSE training puts more emphasis on T_1 . The biggest difference is observed in the estimates of T_2^f , where the CRB-based network performs substantially better compared to the MSE-based network: In the globus pallidus (green arrow in Fig. 8) and the thalamus (blue arrow in Fig. 8), the NLLS and CRB-based network estimations show short T_2^f relaxation times as a result of iron deposition [36, 46]. The MSE-based network is not able to capture this signal variation. These findings are also in line with our conceptual and numerical analysis of the networks, which suggested that the MSE-based network performs particularly poorly in T_2^f .

4 Discussion

As neural networks are increasingly being used to fit biophysical models to MRI data, the need for tailored methods becomes more apparent. Here, we took on the task of finding a training loss that delivers robustness even in heterogeneous parameter spaces. We found that off-the-shelf loss functions like the mean squared error over-emphasize estimates that have large values or naturally have a large error, e.g., because the parameter, at this particular value, is not well encoded by the pulse sequence. The precision with which a parameter is encoded is characterized by the Cramér-Rao bound (CRB) and we demonstrated in this paper that normalizing the squared error of each estimate by respective CRB balances the individual contributions to the training loss.

This normalization of the squared error with the CRB is not entirely heuristic, but rather follows some theoretical concepts: first, it makes the loss of each parameter dimensionless, which allows for adding up the loss of multiple parameters. Second, it normalizes the loss by the one of a maximally efficient unbiased estimator, which provides an absolute evaluation metric for a network; and the networks we trained with the CRB-loss indeed converged approximately to the one of a maximally efficient unbiased estimator.

In order to confirm that our network indeed approximates this ideal condition, we analyzed the bias and the variance of the estimates. We found that the bias of the network trained with the CRB-loss is indeed small (Figs. 2, 3, 5-7) and that the noise variance closely resembles the CRB (Figs. 2 and 4), which indicates that the CRB-based network indeed approximates a maximally-efficient unbiased estimator. Further, we found that this approximation is much better compared to a network that was trained with the MSE-loss.

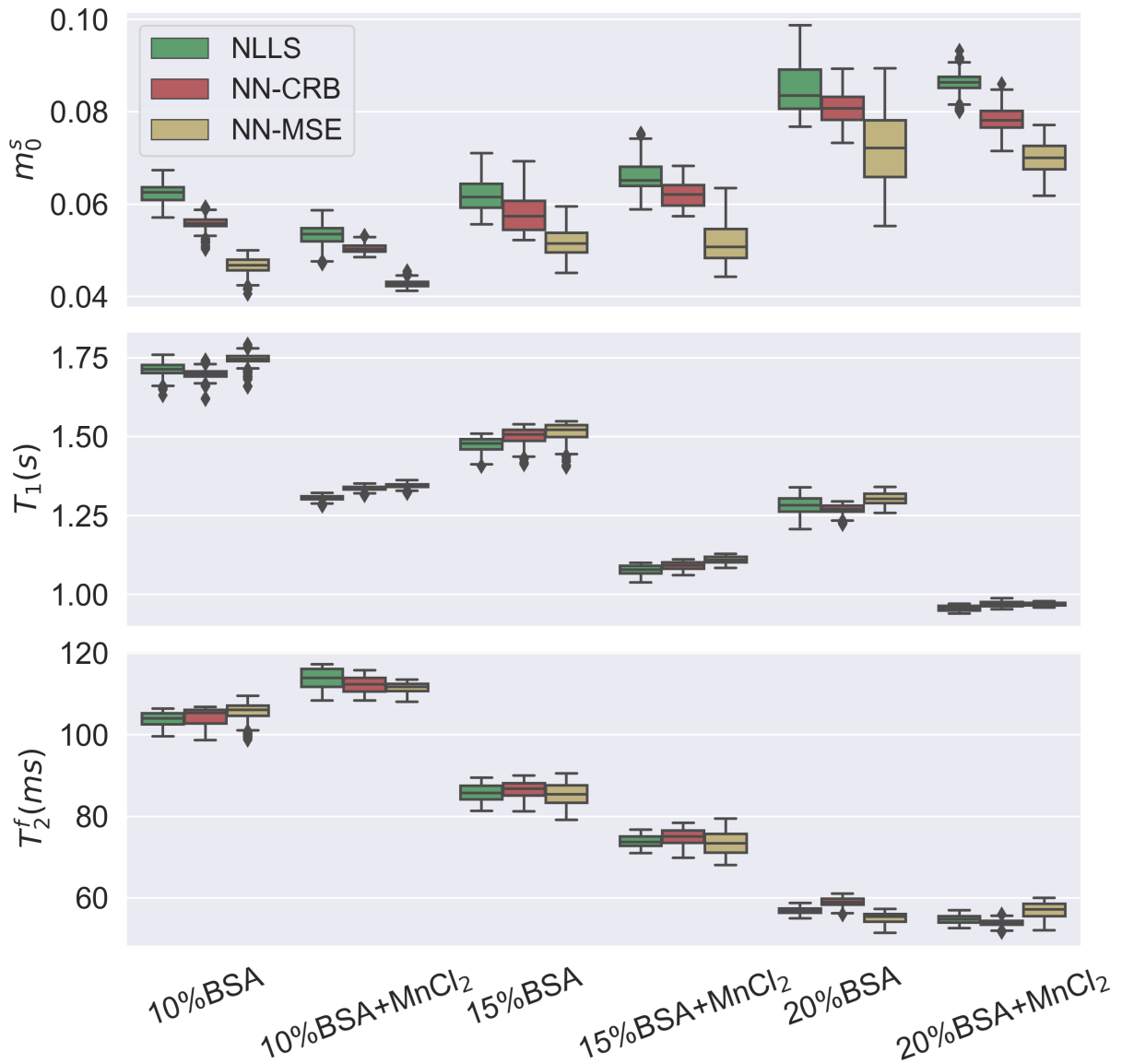


Figure 7: Estimates of m_0^s , T_1 , and T_2^f from a custom phantom containing different concentrations of thermally cross-linked bovine serum albumin (BSA), half of them doped with MnCl₂. The three methods analyzed here show overall good agreement, but the neural network (NN) trained with the CRB loss is consistently in better agreement with the non-linear least square (NLLS) fits, which we consider the gold standard.

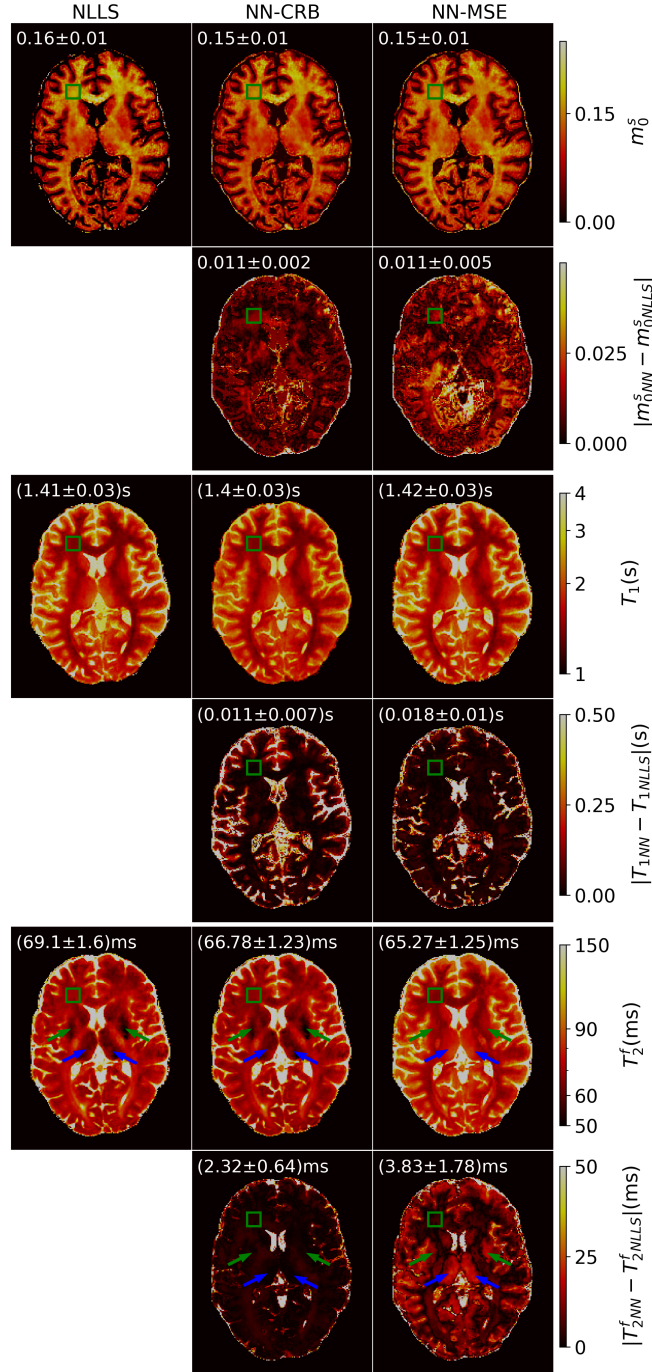


Figure 8: A transversal slice through 3D in vivo maps of m_0^s , T_1 and T_2^f , estimated with non-linear least square (NLLS) fitting, a neural network trained the CRB-loss (NN-CRB) and with the MSE-loss (NN-MSE) respectively. The biggest deviations are observed in T_2^f between MSE-based network estimates and NLLS estimates, which we consider the gold standard. The green arrows point to the globus pallidus and the blue arrows point to the thalamus. The MSE-based network does not capture the short T_2^f relaxation times resulting from the iron deposition in those regions. The green rectangle indicates a frontal white matter region of interest (ROI). The mean and standard deviation of the estimates in this ROI can be found in the top left corner of each subfigure.

Here, we tested the CRB-loss function at the example of an 8-parameter magnetization transfer model [26]. The theoretical foundation of the proposed loss function gives us reason to believe that it results in superior performance for

any model, but the necessity for a well-balanced loss function certainly grows with the heterogeneity of the parameter space or, more precisely, with increasing variations of the Cramér-Rao bound between different parameters and/or throughout the parameter space.

We calculated here the CRB assuming independent and identically distributed Gaussian noise, an assumption that is also implicitly baked into the MSE loss. In order to approximately fulfill this assumption, we reconstructed images into a low rank space spanned by the SVD of the training data [41, 4] and used a combination of parallel imaging [39, 37] and locally low rank flavored compressed sensing [29, 1, 41] to virtually remove the undersampling artifacts. This allows us to train the network with additive Gaussian noise rather than relying on a heuristic noise statistics that emulate undersampling artifacts[44, 45].

To conclude, we have introduced a theoretically well-founded loss function for deep-learning-based method of parameter estimation in quantitative MRI, and demonstrated its superior performance when compared to the commonly used MSE loss function.

References

- [1] Local versus Global Low-Rank Promotion in Dynamic MRI Series Reconstruction. *Proc Intl Soc Mag Reson Med*, 24(7):4371, 2011.
- [2] A. F. Agarap. Deep learning using rectified linear units (relu). *arXiv preprint arXiv:1803.08375*, 2018.
- [3] J. Assländer. A Perspective on MR Fingerprinting. *J. Magn. Reson. Imaging*, 53(3):676–685, mar 2021.
- [4] J. Assländer, M. A. Cloos, F. Knoll, D. K. Sodickson, J. Hennig, and R. Lattanzi. Low rank alternating direction method of multipliers reconstruction for mr fingerprinting. *Magnetic resonance in medicine*, 79(1):83–96, 2018.
- [5] J. Assländer, R. Lattanzi, D. K. Sodickson, and M. A. Cloos. Optimized quantification of spin relaxation times in the hybrid state. *Magnetic Resonance in Medicine*, 82(4):1385–1397, 2019.
- [6] J. Assländer, D. S. Novikov, R. Lattanzi, D. K. Sodickson, and M. A. Cloos. Hybrid-state free precession in nuclear magnetic resonance. *Communications Physics*, 2(1), 2019.
- [7] F. Balsiger, A. S. Konar, S. Chikop, V. Chandran, O. Scheidegger, S. Geethanath, and M. Reyes. Magnetic resonance fingerprinting reconstruction via spatiotemporal convolutional neural networks. In *International Workshop on Machine Learning for Medical Image Reconstruction*, pages 39–46. Springer, 2018.
- [8] F. Barkhof. The clinico-radiological paradox in multiple sclerosis revisited. *Current opinion in neurology*, 15(3):239–245, 2002.
- [9] F. Boux, F. Forbes, J. Arbel, and E. L. Barbier. Dictionary-Free MR Fingerprinting Parameter Estimation Via Inverse Regression. In *Joint Annual Meeting ISMRM-ESMRMB 2018*, Proceedings of Joint Annual Meeting ISMRM-ESMRMB 2018, pages 1–2, Paris, France, June 2018.
- [10] S. F. Cauley, K. Setsompop, D. Ma, Y. Jiang, H. Ye, E. Adalsteinsson, M. A. Griswold, and L. L. Wald. Fast group matching for mr fingerprinting reconstruction. *Magnetic resonance in medicine*, 74(2):523–528, 2015.
- [11] R. W. Chan, E. A. Ramsay, C. H. Cunningham, and D. B. Plewes. Temporal stability of adaptive 3D radial MRI using multidimensional golden means. *Magn. Reson. Med.*, 61(2):354–363, feb 2009.
- [12] O. Cohen, B. Zhu, and M. S. Rosen. Mr fingerprinting deep reconstruction network (drone). *Magnetic resonance in medicine*, 80(3):885–894, 2018.
- [13] H. Cramer. Princeton university press; princeton, nj: 1946. *Mathematical Methods of Statistics.*[Google Scholar].
- [14] M. Davies, G. Puy, P. Vandergheynst, and Y. Wiaux. A compressed sensing framework for magnetic resonance fingerprinting. *Siam journal on imaging sciences*, 7(4):2623–2656, 2014.
- [15] Z. Fang, Y. Chen, S.-C. Hung, X. Zhang, W. Lin, and D. Shen. Submillimeter mr fingerprinting using deep learning-based tissue quantification. *Magnetic resonance in medicine*, 84(2):579–591, 2020.
- [16] Z. Fang, Y. Chen, M. Liu, L. Xiang, Q. Zhang, Q. Wang, W. Lin, and D. Shen. Deep learning for fast and spatially constrained tissue quantification from highly accelerated data in magnetic resonance fingerprinting. *IEEE transactions on medical imaging*, 38(10):2364–2374, 2019.
- [17] S. Flassbeck and J. Assländer. Minimization of eddy current related artefacts in hybrid-state sequences. In *Proceedings of the 2021 ISMRM and SMRT annual meeting and exhibition, year=2021*.
- [18] M. Golbabaee, D. Chen, P. A. Gómez, M. I. Menzel, and M. E. Davies. Geometry of deep learning for magnetic resonance fingerprinting. In *ICASSP 2019-2019 IEEE International Conference on Acoustics, Speech and Signal Processing (ICASSP)*, pages 7825–7829. IEEE, 2019.

- [19] P. A. Gómez, M. Cencini, M. Golbabae, R. F. Schulte, C. Pirkl, I. Horvath, G. Fallo, L. Peretti, M. Tosetti, B. H. Menze, et al. Rapid three-dimensional multiparametric mri with quantitative transient-state imaging. *Scientific reports*, 10(1):1–17, 2020.
- [20] J. I. Hamilton and N. Seiberlich. Machine learning for rapid magnetic resonance fingerprinting tissue property quantification. *Proceedings of the IEEE*, 108(1):69–85, 2019.
- [21] K. He, X. Zhang, S. Ren, and J. Sun. Deep residual learning for image recognition. In *Proceedings of the IEEE conference on computer vision and pattern recognition*, pages 770–778, 2016.
- [22] R. M. Henkelman, X. Huang, Q.-S. Xiang, G. Stanisz, S. D. Swanson, and M. J. Bronskill. Quantitative interpretation of magnetization transfer. *Magnetic resonance in medicine*, 29(6):759–766, 1993.
- [23] E. Hoppe, G. Körzdörfer, M. Nittka, T. Würfl, J. Wetzl, F. Lugauer, and M. Schneider. Deep learning for magnetic resonance fingerprinting: Accelerating the reconstruction of quantitative relaxation maps. In *Proceedings of the 26th Annual Meeting of ISMRM, Paris, France*, 2018.
- [24] E. Hoppe, G. Körzdörfer, T. Würfl, J. Wetzl, F. Lugauer, J. Pfeuffer, and A. K. Maier. Deep learning for magnetic resonance fingerprinting: A new approach for predicting quantitative parameter values from time series. *Studies in health technology and informatics*, 243, 2017.
- [25] E. Hoppe, G. Körzdörfer, T. Würfl, J. Wetzl, F. Lugauer, J. Pfeuffer, and A. K. Maier. Deep learning for magnetic resonance fingerprinting: A new approach for predicting quantitative parameter values from time series. In *GMDS*, pages 202–206, 2017.
- [26] D. K. S. Jakob Assländer. Quantitative magnetization transfer imaging in the hybrid state. 2019.
- [27] I. O. Jelescu, J. Veraart, E. Fieremans, and D. S. Novikov. Degeneracy in model parameter estimation for multi-compartmental diffusion in neuronal tissue. *NMR in Biomedicine*, 29(1):33–47, 2016.
- [28] D. P. Kingma and J. Ba. Adam: A method for stochastic optimization. *arXiv preprint arXiv:1412.6980*, 2014.
- [29] M. Lustig, D. L. Donoho, J. M. Santos, and J. M. Pauly. Compressed sensing MRI. *Signal Process. Mag. IEEE*, 25(2):72–82, 2008.
- [30] D. Ma, V. Gulani, N. Seiberlich, K. Liu, J. L. Sunshine, J. L. Duerk, and M. A. Griswold. Magnetic resonance fingerprinting. *Nature*, 495(7440):187–192, 2013.
- [31] S. J. Matzat, J. van Tiel, G. E. Gold, and E. H. Oei. Quantitative mri techniques of cartilage composition. *Quantitative imaging in medicine and surgery*, 3(3):162, 2013.
- [32] G. Mazor, L. Weizman, A. Tal, and Y. C. Eldar. Low-rank magnetic resonance fingerprinting. *Medical physics*, 45(9):4066–4084, 2018.
- [33] D. F. McGivney, E. Pierre, D. Ma, Y. Jiang, H. Saybasili, V. Gulani, and M. A. Griswold. Svd compression for magnetic resonance fingerprinting in the time domain. *IEEE transactions on medical imaging*, 33(12):2311–2322, 2014.
- [34] G. Nataraj, J. Nielsen, C. Scott, and J. A. Fessler. Dictionary-free mri perk: Parameter estimation via regression with kernels. *IEEE Transactions on Medical Imaging*, 37(9):2103–2114, 2018.
- [35] I. Oksuz, G. Cruz, J. Clough, A. Bustin, N. Fuin, R. M. Botnar, C. Prieto, A. P. King, and J. A. Schnabel. Magnetic resonance fingerprinting using recurrent neural networks. In *2019 IEEE 16th International Symposium on Biomedical Imaging (ISBI 2019)*, pages 1537–1540. IEEE, 2019.
- [36] P. Péran, A. Cherubini, G. Luccichenti, G. Hagberg, J.-F. Démonet, O. Rascol, P. Celsis, C. Caltagirone, G. Spalletta, and U. Sabatini. Volume and iron content in basal ganglia and thalamus. *Human brain mapping*, 30(8):2667–2675, 2009.
- [37] K. P. Pruessmann, M. Weiger, P. Börner, and P. Boesiger. Advances in sensitivity encoding with arbitrary k-space trajectories. *Magn. Reson. Med.*, 46(4):638–651, 2001.
- [38] C. R. Rao. Information and the accuracy attainable in the estimation of statistical parameters. In *Breakthroughs in statistics*, pages 235–247. Springer, 1992.
- [39] D. K. Sodickson and W. J. Manning. Simultaneous acquisition of spatial harmonics (SMASH): Fast imaging with radiofrequency coil arrays. *Magn. Reson. Med.*, 38(4):591–603, 1997.
- [40] P. Song, Y. C. Eldar, G. Mazor, and M. R. Rodrigues. Hydra: Hybrid deep magnetic resonance fingerprinting. *Medical physics*, 46(11):4951–4969, 2019.
- [41] J. I. Tamir, M. Uecker, W. Chen, P. Lai, M. T. Alley, S. S. Vasanawala, and M. Lustig. T2 shuffling: sharp, multicontrast, volumetric fast spin-echo imaging. *Magnetic resonance in medicine*, 77(1):180–195, 2017.

- [42] P. Tofts. *Quantitative MRI of the brain: measuring changes caused by disease*. John Wiley & Sons, 2005.
- [43] M. Uecker and M. Lustig. Bart toolbox for computational magnetic resonance imaging, 2016. doi: 10.5281/zenodo.592960.
- [44] P. Virtue, X. Y. Stella, and M. Lustig. Better than real: Complex-valued neural nets for mri fingerprinting. In *2017 IEEE international conference on image processing (ICIP)*, pages 3953–3957. IEEE, 2017.
- [45] P. Virtue, J. I. Tamir, M. Doneva, S. X. Yu, and M. Lustig. Learning contrast synthesis from mr fingerprinting. In *Proc. 26th Annu. Meeting (ISMRM). icsi. berkeley. edu*, page 676, 2018.
- [46] A. J. Walsh, G. Blevins, R. M. Lebel, P. Seres, D. J. Emery, and A. H. Wilman. Longitudinal mr imaging of iron in multiple sclerosis: an imaging marker of disease. *Radiology*, 270(1):186–196, 2014.
- [47] Z. Wang, H. Li, Q. Zhang, J. Yuan, and X. Wang. Magnetic resonance fingerprinting with compressed sensing and distance metric learning. *Neurocomputing*, 174:560–570, 2016.
- [48] S. Winkelmann, T. Schaeffter, T. Koehler, H. Eggers, and O. Doessel. An Optimal Radial Profile Order Based on the Golden Ratio for Time-Resolved MRI. *IEEE Trans. Med. Imaging*, 26(1):68–76, jan 2007.
- [49] Y. Wu and K. He. Group normalization. In *Proceedings of the European conference on computer vision (ECCV)*, pages 3–19, 2018.
- [50] M. Yang, D. Ma, Y. Jiang, J. Hamilton, N. Seiberlich, M. A. Griswold, and D. McGivney. Low rank approximation methods for mr fingerprinting with large scale dictionaries. *Magnetic resonance in medicine*, 79(4):2392–2400, 2018.
- [51] B. Zhao, J. P. Haldar, K. Setsompop, and L. L. Wald. Optimal experiment design for magnetic resonance fingerprinting. In *2016 38th Annual International Conference of the IEEE Engineering in Medicine and Biology Society (EMBC)*, pages 453–456. IEEE, 2016.

Supplementary Material

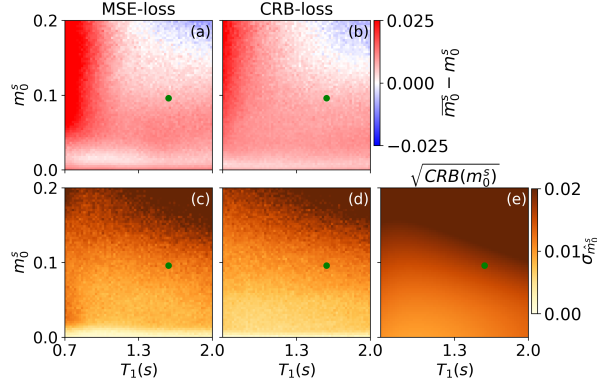


Figure 9: Bias (a,b) and standard deviation (c,d) of \hat{m}_0^s , estimated with the network trained with the MSE-loss and CRB-loss, respectively. The latter is compared to the square root of the Cramér-Rao bound (e), which provides a theoretical limit for an unbiased estimator. The green dots indicate the mean values of the corresponded parameters in the training dataset. The maps were generated with the test dataset #2.

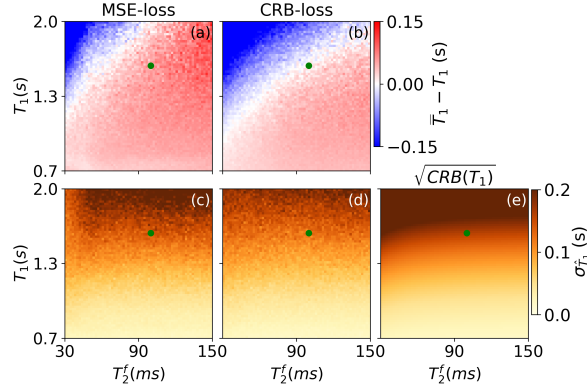


Figure 10: Bias (a,b) and standard deviation (c,d) of \hat{T}_1 , estimated with the network trained with the MSE-loss and CRB-loss, respectively. The latter is compared to the square root of the Cramér-Rao bound (e), which provides a theoretical limit for an unbiased estimator. The green dots indicate the mean values of the corresponded parameters in the training dataset. The maps were generated with the test dataset #2.

When using the network trained with the CRB-loss, the bias of the T_1 estimation (Supplementary Fig. 10b) with the CRB-based network is slightly larger (0.11 on average of absolute bias) than that of the MSE-based network (Fig. 10a; 0.07 on average), which is in line with the hypothesis that the MSE loss puts more emphasis on T_1 . The bias of the m_0^s estimation with the CRB-based network in a slice spanned by m_0^s and T_1 (Fig. 9b) is slightly smaller (0.0053 on average of absolute bias) than that of the MSE-based network (Fig. 9a; 0.0065 on average). Overall, the two networks have similar performance in estimating m_0^s and T_1 , while we do observe a substantial difference in the performance in estimating T_2^f .